



RESEARCH LETTER

10.1002/2017GL072945

Key Points:

- Analysis indicates significant reduction in summertime upwelling for much of the California Current
- Forced response is not clearly evident until the second half of the 21st century due to internal variability
- Trends identified in historical observations are unlikely to be the result of anthropogenic forcing

Supporting Information:

- Supporting Information S1

Correspondence to:

R. X. Brady,
riley.brady@colorado.edu

Citation:

Brady, R. X., M. A. Alexander, N. S. Lovenduski, and R. R. Rykaczewski (2017), Emergent anthropogenic trends in California Current upwelling, *Geophys. Res. Lett.*, *44*, 5044–5052, doi:10.1002/2017GL072945.

Received 3 FEB 2017

Accepted 1 MAY 2017

Accepted article online 4 MAY 2017

Published online 29 MAY 2017

Emergent anthropogenic trends in California Current upwelling

Riley X. Brady¹ , Michael A. Alexander², Nicole S. Lovenduski¹ , and Ryan R. Rykaczewski³ 

¹Department of Atmospheric and Oceanic Sciences and Institute of Arctic and Alpine Research, University of Colorado Boulder, Boulder, Colorado, USA, ²Physical Sciences Division, NOAA Earth System Research Laboratory, Boulder, Colorado, USA, ³Department of Biological Sciences and Marine Science Program, University of South Carolina, Columbia, South Carolina, USA

Abstract Upwelling in the California Current System (CCS) sustains a productive ecosystem and is mediated by alongshore, equatorward wind stress. A decades-old hypothesis proposes that global warming will accelerate these upwelling favorable winds. Recent analyses provide empirical support for upwelling intensification in the poleward portion of the CCS. However, these studies rely on proxies for upwelling and are limited in their ability to distinguish anthropogenic forcing from internal climate variability. Here we estimate simulated changes in CCS upwelling from 1920 to 2100 using monthly output from a single climate model ensemble, where divergences among simulations can be attributed entirely to internal climate variability. Our projections suggest that CCS upwelling will become more intense in the spring and less intense in the summer as a result of anthropogenic climate change. Anthropogenic changes in upwelling will emerge primarily in the second half of the century.

1. Introduction

Upwelling in the California Current System (CCS) replenishes surface waters that are forced offshore through Ekman transport in response to equatorward (“upwelling favorable”) alongshore winds (\bar{u}_a) [Huyer, 1983]. These winds are mediated by an atmospheric pressure gradient between the North Pacific High (NPH) and Continental Low. The nutrient-rich upwelled waters serve as a fertilizer for phytoplankton, fueling populations of commercially valuable fish [Ryther *et al.*, 1969; Rykaczewski and Checkley, 2008]; thus, the response of CCS upwelling to climate change is of concern for future food security and the overall health of the ecosystem.

Bakun [1990] suggested that the coastal upwelling process is sensitive to anthropogenic climate change, as coastal landmasses are anticipated to warm more quickly than the neighboring ocean. *Bakun* [1990] hypothesized that this increased surface temperature difference would intensify onshore-offshore pressure gradients and accelerate \bar{u}_a . This hypothesis has spurred a number of investigations, which are reviewed by *García-Reyes et al.* [2015]. In summary, consensus has not yet been reached regarding historical trends in \bar{u}_a , due to the short time series and noisiness associated with coastal wind data, as well as inconsistencies in researchers’ temporal definition of upwelling seasons [García-Reyes *et al.*, 2015]. However, for the CCS in particular, *García-Reyes and Largier* [2010] suggest a long-term increase in \bar{u}_a for March–July from 1982 to 2008 along central California. *Narayan et al.* [2010] report some evidence of an annual increase in upwelling favorable alongshore wind stress (τ_a) from 1960 to 2001 for much of California. Lastly, *Sydeman et al.* [2014]’s meta-analysis of 22 studies using modeled and observed wind trends over the past six decades finds significant agreement with *Bakun* [1990]’s \bar{u}_a intensification hypothesis in the poleward portion of the CCS during the “warm season,” which spans May–August.

Rykaczewski et al. [2015] and *Wang et al.* [2015] used “ensembles-of-opportunity,” composed of a number of global Atmosphere–Ocean General Circulation Models (AOGCMs) from the Fifth Coupled Model Intercomparison Project (CMIP5) to investigate climate change-induced trends in coastal upwelling in the major eastern boundary currents. In the CCS, *Rykaczewski et al.* [2015] find that a majority of CMIP5 models project a significant weakening of summertime τ_a in the equatorward portion of the system, with nonsignificant change projected for the poleward portion. Only in monthly averages of April and May do they find a significant intensification of τ_a . *Wang et al.* [2015] use Ekman transport at daily resolution (calculated via \bar{u}_a and the standard

bulk aerodynamic formula) as a proxy for upwelling. The only significant change they projected is a trend of weakening Ekman transport in the Southern California Bight, with no significant change elsewhere in the CCS.

While previous studies have provided insight into the possible future of upwelling systems under climate change, such attempts have been limited in their ability to distinguish anthropogenic forcing from internal climate variability. This is because each CMIP5 model projection is influenced by anthropogenic forcing, internal climate variability, and model structure [Hawkins and Sutton, 2009]. Thus, in multimodel studies, the impacts of these three sources of uncertainty cannot be reliably distinguished [Solomon *et al.*, 2011]. To address this concern, modeling institutions have begun to develop single model “large ensembles,” which consist of numerous independent runs separated only by minor differences in their initial atmospheric state and run under a common radiative forcing scenario [e.g., Kay *et al.*, 2015]. Because simulations with large ensembles use a single climate model and common emission scenario, disparities between simulations are attributed entirely to internal variability. Thus, using this experiment design, one can assess the magnitude of the forced anthropogenic “signal” relative to the “noise” of internal climate variability to provide a probabilistic projection of climate change impacts in a system with internal variability.

In this study, we will use a large ensemble that is forced by historical emissions and the RCP 8.5 radiative forcing scenario [Riahi *et al.*, 2011] to address the impacts of anthropogenic climate change—relative to internal climate variability—on upwelling in the CCS over 1920–2100. We consider trends at a monthly resolution to avoid inconsistencies in the temporal definition of the upwelling season and investigate vertical velocity (\bar{w}) to directly project changes to ocean upwelling rather than using τ_a as a proxy. We are interested in examining whether anthropogenic impacts are expected to be “emergent” over the next century in the CCS, given potentially large internal variability in upwelling.

2. Data and Methods

2.1. Numerical Model

We utilize monthly output from 40 members of the Community Earth System Model Large Ensemble Project (CESM-LE), which is documented extensively in Kay *et al.* [2015] and further described in Lovenduski *et al.* [2016]. Each ensemble member begins from a slightly different initial atmospheric temperature in 1920, is subject to historical radiative forcing through 2005, and then RCP 8.5 radiative forcing is applied from 2006 to 2100 [Riahi *et al.*, 2011].

Output from this study was generated over the $1^\circ \times 1^\circ$ Parallel Ocean Program version 2 (POP2) grid [Smith *et al.*, 2010], the ocean component of the CESM, which has a vertical resolution of 10 m through the upper 250 m, thereby resolving the Ekman layer. We use \bar{w} at 50 m depth as our primary metric for coastal upwelling. This differs from previous studies that compute a coastal upwelling index [Bakun, 1973] via cross-shore atmospheric pressure fields or consider τ_a values as a proxy for upwelling intensity. Here changes in \bar{w} represent changes in upwelling due to both Ekman processes and the net onshore geostrophic flow of water [Marchesiello and Estrade, 2010; Jacox *et al.*, 2014]. We assess the model's ability to represent the observed seasonal cycle in wind stress by comparing the long-term historical climatology of the CESM-LE surface ocean wind stress (τ_x, τ_y) to τ_a observations in the CCS.

Figure 1c displays our model domain, which represents a portion of the CCS. It spans from 30°N to 45°N and is split into northern, central, and southern regions, with boundaries between these regions at the model's representation of Point Conception (34.4°N) and Cape Mendocino (40.4°N) [Dorman and Winant, 1995; Jacox *et al.*, 2014]. \bar{w} values were retrieved from the first offshore grid cell to establish a monthly time series for each region. Projections of τ_x and τ_y onto a line parallel with the given region's average coastline orientation were used in deriving τ_a (see Figure 1c). A monthly τ_a index was computed by taking the area-weighted average of τ_a for two grid cells in the cross-shore direction throughout the alongshore expanse of each region, to compensate for the weak winds caused by friction over the coastline [Small *et al.*, 2015].

2.2. Statistical Methods

To quantify change over time, an epoch difference was calculated from two 30 year periods, spanning 1925–1954 and 2071–2100. We began the historical epoch 6 years after the initiation of the model to avoid artificial reduction in the spread of the ensemble due to the memory of ocean initial conditions [Deser *et al.*, 2012].

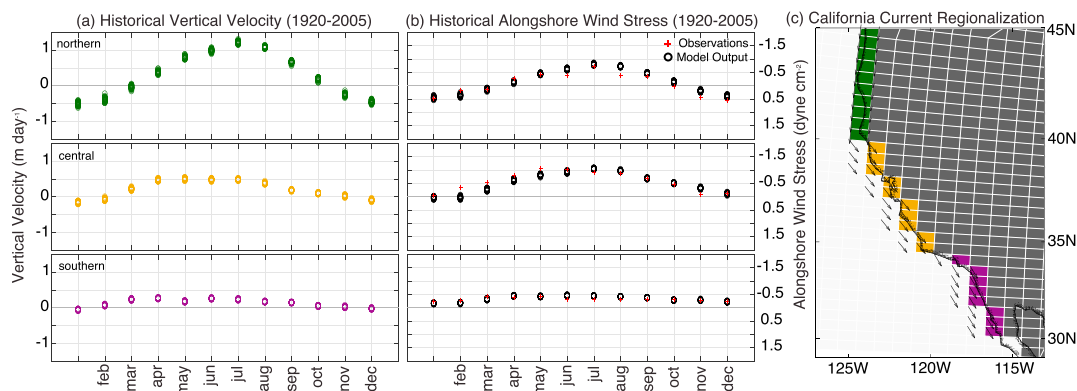


Figure 1. (a) Historical mean (1920–2005) \bar{w} (m day^{-1}) and (b) historical mean alongshore wind stress (dyne cm^{-2}) by month and region. Colored circles show individual ensemble members; red crosses show observations from Nelson [1977]. (c) Model grid and regions analyzed in this study. Colored cells indicate ocean grid cells for which vertical velocity was analyzed (colors correspond to regions from Figure 1a), while vectors designate the locations and directions over which alongshore winds were evaluated.

For each month and region, 40 individual epoch differences of \bar{w} —one for each ensemble member—were calculated. The ensemble mean epoch difference (X) was considered to be the *forced* signal. This is the component of change shared by all ensemble members due to external anthropogenic forcing. The standard deviation of individual epoch differences around that mean (σ) was considered to be the noise or the component of change due to *internal* climate variability. We compute a signal-to-noise ratio (SNR) for each case, where a SNR of 2 (equation (1)) or greater was deemed a statistically significant emergence of the forced signal through 2100, as derived from the t test assuming 95% significance [Deser et al., 2014; Thompson et al., 2015]:

$$\text{SNR} = \frac{X}{\sigma} \geq 2 \quad (1)$$

We used a time of emergence (TOE) analysis to quantify the specific year in which a statistically significant forced signal is expected to emerge for a given month and region. Following McKinley et al. [2016], we computed linear regressions on \bar{w} for each month and region in each simulation for cumulative 5 year intervals (i.e., 1920–1925, 1920–1930, 1920–1935, ..., 1920–2100). We considered the TOE to be the last year of the interval in which the SNR exceeded a value of 2 for that interval and all subsequent intervals.

We approximated the minimum number of simulations required to reach a 95% confidence level in our detection of the forced signal for each month and region (N_{\min}). If N_{\min} was found to be larger than 40 (the number of simulations available in the CESM-LE), we excluded that month and region from our analysis. We computed N_{\min} following the methodology outlined in Deser et al. [2012]

$$N_{\min} = \frac{8}{\left(\frac{X}{\sigma}\right)^2} \quad (2)$$

2.3. Wind Stress Observations

To evaluate model skill in representing historical climatological τ_a , we use data from Nelson [1977], which provides $1^\circ \times 1^\circ$ monthly fields of surface wind stress in the CCS from approximately one million ship-board observations over 1857–1972. τ_a magnitudes from the first offshore grid cell were averaged over the aforementioned northern, central, and southern regions to produce a historical climatology of the region.

3. Results and Discussion

The historical climatologies of modeled \bar{w} and τ_a for each region are displayed in Figures 1a and 1b, along with observational climatology for τ_a from Nelson [1977]. Ensemble variability in both \bar{w} and τ_a is small in all regions across each month in the CCS (as illustrated by the spread of individual circles on each panel), as the 85 year averages (1920–2005) provide a robust estimate of the model’s mean climate in the three regions. Each region displays a distinct seasonality in both the onset and intensity of \bar{w} (Figure 1a): the southern region exhibits persistent annual, low-magnitude upwelling; the central region exhibits positive upwelling

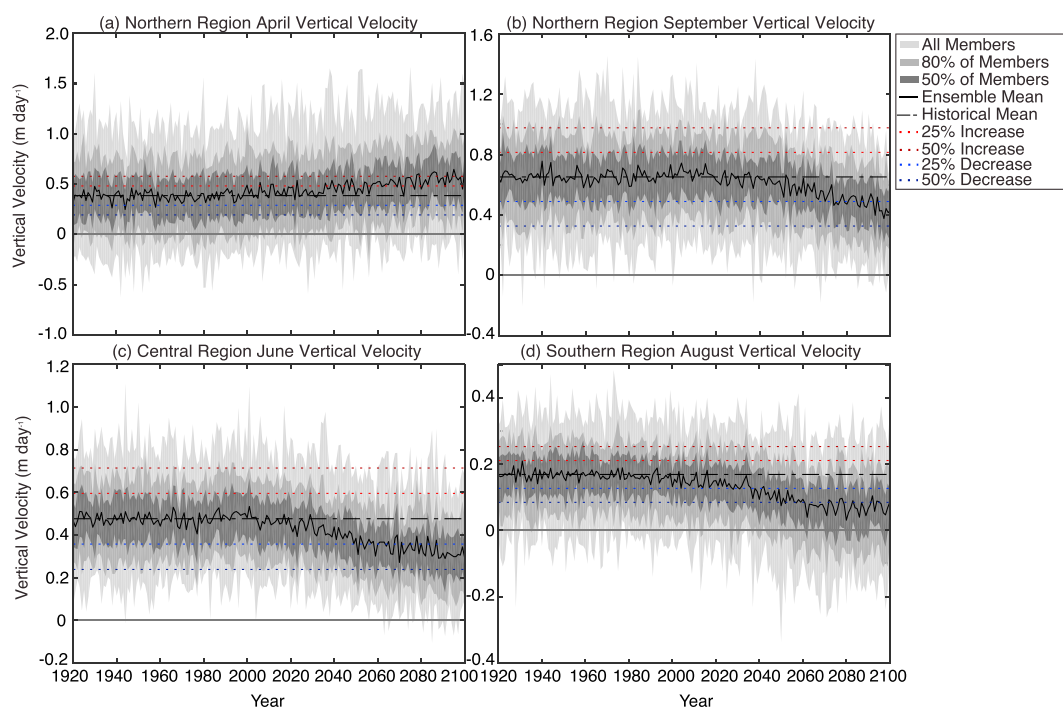


Figure 2. Temporal evolution of the modeled monthly mean vertical velocity (m day^{-1}) over the (a) northern region in April, (b) northern region in September, (c) central region in June, and (d) southern region in August. Light gray shading indicates the spread across the 40 ensemble members; medium and dark gray shading shows the spread across the inner 80% and 50% of the range, respectively. Black solid line indicates the ensemble mean, and black dashed lines indicate the historical mean (1925–1954). Light red and blue dashed lines indicate a 25% increase and decrease in vertical velocity, relative to the historical mean, respectively, and dark red and blue dashed lines indicate a 50% change relative to the historical mean, respectively. Note that the y axes differ in each case to highlight the magnitude of ensemble spread.

beginning in March and ending in October, with a relatively moderate and stable magnitude of \bar{w} ; and upwelling in the northern region begins latest—in April—but displays the highest magnitude upwelling that peaks in July and dissipates in October.

Modeled τ_a displays similar seasonality as \bar{w} over each region (Figure 1b). Further, observed winds show reasonable agreement with the seasonal progression of the model in both onset and magnitude. Such an agreement suggests that (1) despite having a coarse spatial resolution, the CESM-LE captures the seasonality and magnitude of upwelling favorable τ_a ; and (2) we have chosen regions characterized by distinct seasonality in alongshore winds [Huyer, 1983].

Figure 2 displays unfiltered time series of \bar{w} for four month-region pairs, which were selected due to their significant change over time seen in Figure 3a, with the ensemble mean (forced signal) depicted as the black line and the spread of ensemble members in varying shades of gray. Note that the y axis scales are different for each subplot to highlight ensemble spread. We find that the forced signal does not progress linearly through time, where there is near-zero change to the system for roughly 80 years, followed by a trend of increasing or decreasing \bar{w} (Figure 2). Also depicted is the high magnitude of internal variability in \bar{w} . For instance, the northern region in April is a climatologically active upwelling zone (Figure 1a), but there is at least one simulation for nearly each year of the time series that models downwelling during this time, as seen by the outer gray band extending below the zero-upwelling line (Figure 2a). Further, one can see a meridional dependency in the magnitude of internal variability. The northern region has large internal variability, with an average ensemble spread of 0.32 m day^{-1} and 0.23 m day^{-1} in April and September, respectively (Figures 2a and 2b). On the other hand, the spread between ensemble members in the central and southern regions is more modest, with a value of 0.15 m day^{-1} in the central region (Figure 2c) and 0.09 m day^{-1} in the southern region

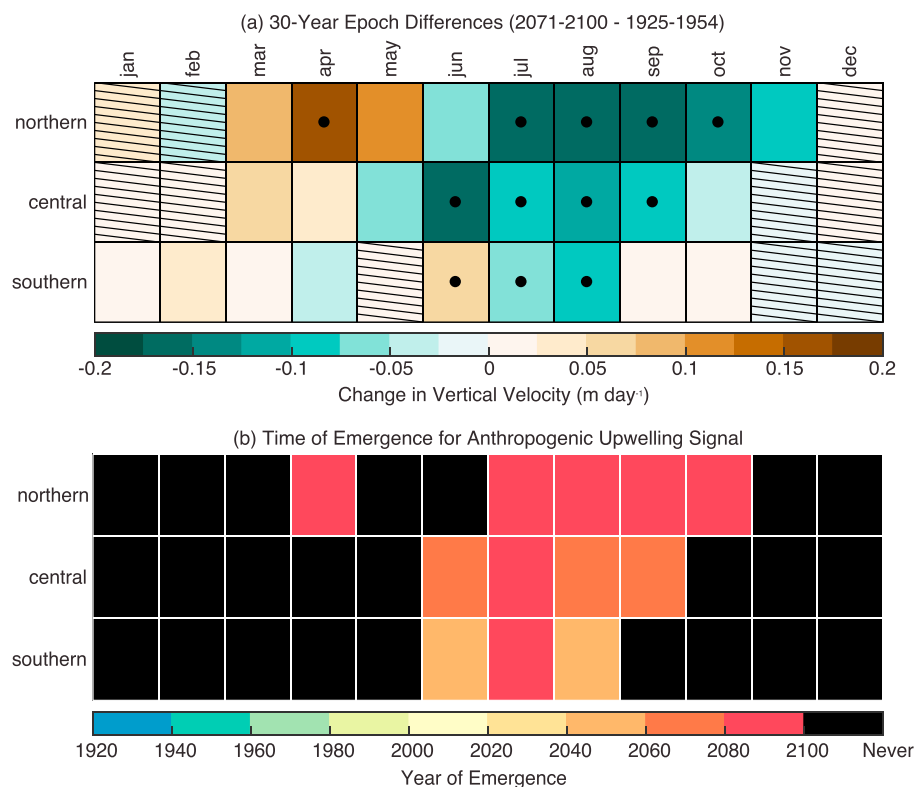


Figure 3. (a) The 30 year epoch differences (2071–2100 – 1925–1954) in \bar{w} by month and region. Black dots denote significant change, where the signal-to-noise ratio is greater than 2 (equation (1)), and hatching indicates that there are not enough ensemble members to detect significant change (equation (2)). (b) Year when forced change in \bar{w} is detectable by month and region, per methodology outlined in section 2.2. Black boxes denote that the change in upwelling is not detectable before 2100.

(Figure 2d). Internal variability increases in the poleward direction for every month (Table 1). Intuitively, these plots suggest a relatively late TOE for each case: the forced signal varies little until ~2020, with a large degree of variability across simulations.

We display the results of our SNR and TOE analyses in Figure 3. Browner shades in Figure 3a indicate a forced intensification of upwelling (positive change in \bar{w}), while bluer shades indicate a relative weakening of upwelling (negative change in \bar{w}). Dots identify cases where the forced signal is expected to be emergent over the length of the time series (equation (1)), and those with hatching are excluded from the analysis as there was less than 95% confidence in the forced signal (equation (2)).

We discover a pattern of intensified \bar{w} in the spring and a reduction of \bar{w} in the summer (Figure 3a). The forced intensification is only significant in the northern region in April and in the southern region in June, while the forced reduction is significant in much of the summer in the central and northern regions and part of the summer in the southern region. The central and northern regions exhibit a more coherent pattern of seasonal change than the southern region across ensemble members. In other words, the southern region does not have as clear a shift between spring intensification and summer reduction of \bar{w} at a monthly resolution. We find the highest uncertainty in the forced signal in the winter months, as denoted by hatching. Raw values for the forced signal, internal variability, SNR, and N_{\min} can be found in Table 1.

Figure 3a illustrates that the sign of significant change in \bar{w} can be seasonally variable but is more likely to result in weakening, rather than intensification, of upwelling. By averaging across warm seasons or the annual cycle, one may miss finer-scale temporal changes to the system. Figure 3b displays the TOE for each month and region, with warmer colors denoting a year of emergence closer to 2100 and black expressing that the change in \bar{w} is not detectable prior to 2100. Here we project that the forced signal will not be emergent in statistically significant month-region pairs until the latter half of this century (Figure 3b). We find the earliest emergence of intensified \bar{w} to be in 2055 in the southern region in June and the earliest of reduced \bar{w} to be

Table 1. The 30 Year Epoch Differences (2071–2100 – 1925–1954) in \bar{w} ^a

	Jan	Feb	Mar	Apr	May	Jun	Jul	Aug	Sep	Oct	Nov	Dec
<i>Northern Region</i>												
Forced ^b	0.04	-0.03	0.09	0.16	0.12	-0.06	-0.15	-0.17	-0.17	-0.13	-0.08	0.01
Internal ^b	0.09	0.11	0.09	0.07	0.07	0.10	0.06	0.05	0.06	0.07	0.10	0.09
Signal-to-noise	0.39	0.24	1.02	2.31	1.70	0.57	2.44	3.32	2.74	2.13	0.84	0.13
Ensemble spread ^b	0.43	0.43	0.35	0.32	0.32	0.31	0.29	0.23	0.23	0.27	0.32	0.39
N_{\min}	>40	>40	8	2	3	25	2	1	2	2	12	>40
TOE	-	-	-	2085	-	-	2090	2080	2090	2095	-	-
<i>Central Region</i>												
Forced ^b	0.01	0.01	0.07	0.04	-0.06	-0.15	-0.10	-0.11	-0.08	-0.04	-0.01	0.01
Internal ^b	0.05	0.06	0.05	0.04	0.04	0.04	0.03	0.03	0.03	0.04	0.04	0.05
Signal-to-noise	0.10	0.25	1.32	1.18	1.53	3.75	2.89	3.62	3.09	1.02	0.13	0.16
Ensemble spread ^b	0.22	0.23	0.20	0.19	0.16	0.15	0.14	0.12	0.11	0.12	0.15	0.18
N_{\min}	>40	>40	5	6	4	1	1	1	1	8	>40	>40
TOE	-	-	-	-	-	2060	2080	2075	2075	-	-	-
<i>Southern Region</i>												
Forced ^b	0.02	0.04	0.02	-0.03	0.00	0.06	-0.07	-0.10	0.02	0.01	-0.01	-0.01
Internal ^b	0.02	0.03	0.03	0.03	0.02	0.03	0.03	0.02	0.02	0.02	0.02	0.03
Signal-to-noise	0.81	1.23	0.59	1.09	0.19	2.19	2.94	4.21	0.66	0.52	0.32	0.20
Ensemble spread ^b	0.11	0.12	0.12	0.11	0.10	0.10	0.10	0.09	0.09	0.09	0.09	0.10
N_{\min}	13	6	24	7	>40	2	1	1	19	30	>40	>40
TOE	-	-	-	-	-	2055	2080	2050	-	-	-	-

^aFor the forced signal, red colors indicate an increase in \bar{w} , while blue colors indicate a decrease in \bar{w} . Internal variability was calculated as the standard deviation of the 40 epoch differences from individual ensemble members. Boldface numbers indicate a statistically significant signal-to-noise ratio. Ensemble spread was computed by taking the average standard deviation of the 40 simulations at each year across the time series. N_{\min} was calculated via equation (2), and the methodology for TOE calculations is outlined in section 2.2. Values are rounded to two digits past the decimal.

^bm day⁻¹.

in 2050 in the southern region in August. No significant forced change in the northern region is expected to emerge until 2080 or later (Table 1).

As highlighted earlier, studies such as *Bakun* [1990], *García-Reyes and Largier* [2010], *Narayan et al.* [2010], and *Sydemann et al.* [2014] suggest that observed historical trends in CCS upwelling may be the result of anthropogenic climate change. However, we find that such trends are unlikely to be distinguishable from internal variability until the second half of the 21st century. To better illustrate this point, we investigate the role of internal variability over the CCS based on linear trends of \bar{w} during the upwelling season spanning April–September from 1946 to 1988, the same time period used by *Bakun* [1990], in Figure 4. The first column is simply the linear trend over the aforementioned time frame for the given simulation, i.e., it can be considered the total trend that would be experienced in the “real world.” We then decomposed the total trend into its internal and forced contributions, as seen in the second and third columns. To do so, we subtracted the ensemble mean (displayed in the third column) from each individual trend to estimate the contribution of internal variability to the total projected trend.

Simulations S02, S14, and S07 are individual, independent runs that were selected from the ensemble to illustrate that internal variability is the dominant factor in determining trends over multidecadal historical time scales (Figure 4). S02 exhibits a positive trend in upwelling that could be interpreted to be consistent with the hypothesis of *Bakun* [1990], as we see a general intensification of \bar{w} along the entire coastline of the CCS. S14 shows a mixed response with latitude, with an intensification in the poleward portion of the CCS, and a weakening in the equatorward portion. S07 depicts nearly the opposite of S02, exhibiting trends of reduced upwelling along the entire coastline of the CCS. We also note variability in trends of offshore, curl-driven upwelling. Overall, we find that internal variability plays a dominant role in the direction and intensity of 40 year historical trends in \bar{w} over this time period. Qualitatively, we can see this by considering that the forced

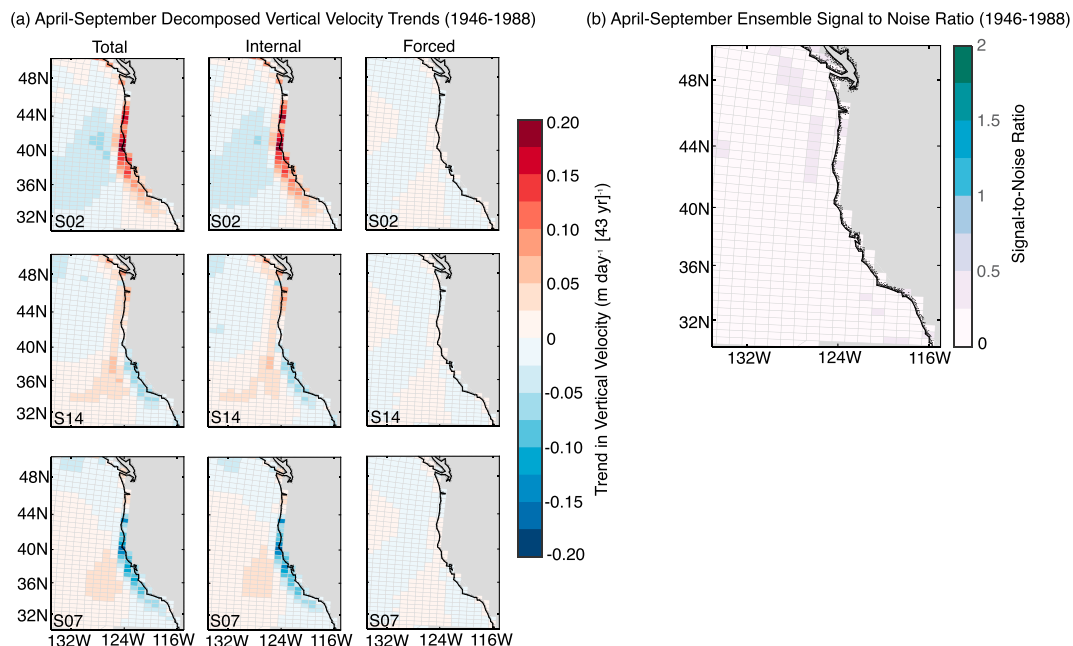


Figure 4. (a) Linear trends in vertical velocity ($\text{m day}^{-1} [43 \text{ yr}]^{-1}$) for three independent ensemble members averaged across April through September over the years 1946–1988. The first column is the total linear trend for each ensemble member, while the next two columns are the total change decomposed into internal and forced contributions, respectively. (b) Signal-to-noise ratio across all 40 ensemble members for April–September over the years 1946–1988.

signal in Figure 4a is small in comparison to the total trend (the total trend is largely reflective of the internal trend). Quantitatively, in Figure 4b, we calculated the SNR for the CCS over this time period, resulting in a $\text{SNR} < 1$ everywhere in the domain. We would expect much higher values, an $\text{SNR} \geq 2$, if these historical changes were the result of external forcing [Deser et al., 2014]. This suggests that the aforementioned studies could have potentially attributed trends of intensifying τ_a to external forcing, when they were instead the result of multidecadal climate variability.

Internal variability is expected to be large enough to obscure the forced signal during many months of the year, even through the end of the 21st century; this is particularly evident in winter and spring (Figure 3a). Throughout the summer, the forced signal is expected to be strong enough to emerge from the noise of internal variability by 2100 (Figure 3a). However, multidecadal climate variability is still large enough to obscure clear identification of the forced signal until after 2050 in months and regions with significant changes due to external forcing (Figure 3b and Table 1). We also note that at a monthly resolution, the sign of change in \bar{w} is seasonally variable (Figure 3a). This is most evident in the northern region, where we project a significant intensification of \bar{w} in April, followed by significant weakening throughout much of the summer. There are a number of physical mechanisms that might lead to changes in upwelling rates. The major contributors are likely the following: (1) thermal stratification of the upper ocean, which would inhibit vertical mixing throughout the CCS [Di Lorenzo et al., 2005; Gruber, 2011; Bakun et al., 2015; García-Reyes et al., 2015]; (2) changes to large-scale atmospheric circulation, such as the poleward expansion of Hadley circulation and shifts in the location of the NPH, which would alter local winds and wind stress curl [Lu et al., 2007; Yin, 2005; Rykaczewski et al., 2015]; and (3) climate-driven changes to remote ocean forcing, e.g., changes to tropical Pacific variability which would affect the influence of coastally trapped waves on upwelling [Engida et al., 2016; Timmermann et al., 1999; Collins et al., 2010].

We find two important changes in the phenology (amplitude and phasing) of CCS upwelling [Bograd et al., 2002, 2009]: (1) a more intense spring transition, which may influence top predators in the ecosystem, and (2) a reduction in total seasonal upwelling, which is likely to impact lower trophic biota (Figure S1 in the supporting information). One phenological event is the spring transition, during which the shift from winter downwelling to spring upwelling induces a dynamical and biological response within weeks [Lynn et al., 2003]. We cannot quantify expected changes to the exact onset day of seasonal upwelling, due to the

temporal resolution of our output. However, we do find that 85% and 93% of simulations project a more intense shift between February downwelling and March upwelling in the northern and central regions, respectively. Variability in the intensity of springtime upwelling has been associated with changes in the productivities of particular populations in the CCS. Earlier transitions to the upwelling season may act to increase the availability of prey for many seabirds and fishes, particularly those with life-history characteristics (e.g., spawning, egg laying, and chick rearing) with high energetic demands during late winter and spring [Black *et al.*, 2011; Thompson *et al.*, 2012; García-Reyes *et al.*, 2013]. However, some top predators are more sensitive to upwelling variability in summer and may not exhibit relationships with the timing of the spring transition [Black *et al.*, 2011]. On the other hand, a reduction in total seasonal upwelling would not necessarily inhibit primary production in the CCS. Moderate levels of upwelling have been suggested to be optimal for nearshore productivity [Cury and Roy, 1989; Botsford *et al.*, 2003; García-Reyes *et al.*, 2014; Jacox *et al.*, 2016]. This is because more intense alongshore wind stress (and thus upwelling) leads to localized deep mixing and offshore advection of lower trophic biota. Thus, a lengthening and “flattening” of seasonal upwelling, which is particularly evident in the northern and central regions (Figure S1), might lead to enhanced nearshore productivity. Changes in productivity will also be dependent upon the characteristics of future source waters [Bakun *et al.*, 2015]. Although thermal stratification might reduce the depth from which waters are upwelled [Chhak and Di Lorenzo, 2007], model projections have suggested that these effects may be counteracted by enhanced nitrate concentrations in source waters [Rykaczewski and Dunne, 2010].

Our conclusions are subject to a few caveats. The spatial resolution of the CESM-LE at $1^\circ \times 1^\circ$ is more coarse than the typical ~ 10 km scale of coastal upwelling. However, the CESM-LE is the best available experiment design for assessing internal climate variability at the time of publication. Further, we expect the coarse \bar{w} from the AOGCM to be broadly representative of combined coastal and curl-driven upwelling processes within the nearshore grid cells [Wang *et al.*, 2015]. Lastly, we assume that the model has a reasonable representation of the seasonality and magnitude of \bar{w} , as there are no observational data sets available of \bar{w} with which to evaluate the model. However, we mediated this concern by indirectly evaluating the modeled upwelling processes through the comparison of the CESM-CAM5 τ_a with an observational data set of τ_a .

This study showcases the need to consider the impacts of internal climate variability on future upwelling in the CCS. Furthermore, studies analyzing changes to the CCS at a daily or monthly resolution—rather than averaging across seasons or the annual cycle—may highlight finer-scale changes to ecosystem structure that may arise due to both cross-shore and alongshore variability in the CCS. Lastly, as more modeling institutions develop large ensembles and make their output publicly available, a multimodel ensemble of large ensembles will allow one not only to assess the influence of internal variability on our ability to identify long-term change in CCS upwelling but also to investigate the sensitivity of projected upwelling changes to model structure.

Acknowledgments

CESM ensemble output is available from the Earth System Grid (<http://www.cesm.ucar.edu/projects/community-projects/LENS/data-sets.html>). CESM computing resources were provided by CISL at NCAR. We thank the National Oceanic and Atmospheric Administration (NOAA), the Office of Undergraduate Research at the University of South Carolina, and the Department of Energy for supporting R.X.B. through the Hollings Scholarship, Magellan Scholarship, and Computational Science Graduate Fellowship (DE-FG02-97ER25308) during this study. Lastly, we thank NSF for funding (grants OCE-1434530 and OCE-1558225).

References

- Bakun, A. (1973), Coastal upwelling indices, West Coast of North America, 1946-71, *Tech. Rep.*, Natl. Mar. Fisheries Serv., Seattle, Wash.
- Bakun, A. (1990), Global climate change and intensification of coastal ocean upwelling, *Science*, 247(4939), 198–201.
- Bakun, A., B. Black, S. J. Bograd, M. Garcia-Reyes, A. Miller, R. Rykaczewski, and W. Sydeman (2015), Anticipated effects of climate change on coastal upwelling ecosystems, *Curr. Clim. Change Rep.*, 1(2), 85–93.
- Black, B. A., I. D. Schroeder, W. J. Sydeman, S. J. Bograd, B. K. Wells, and F. B. Schwing (2011), Winter and summer upwelling modes and their biological importance in the California current ecosystem, *Global Change Biol.*, 17(8), 2536–2545.
- Bograd, S., F. Schwing, R. Mendelsohn, and P. Green-Jessen (2002), On the changing seasonality over the North Pacific, *Geophys. Res. Lett.*, 29(9), 1333, doi:10.1029/2001GL013790.
- Bograd, S. J., I. Schroeder, N. Sarkar, X. Qiu, W. J. Sydeman, and F. B. Schwing (2009), Phenology of coastal upwelling in the California Current, *Geophys. Res. Lett.*, 36, L01602, doi:10.1029/2008GL035933.
- Botsford, L. W., C. A. Lawrence, E. P. Dever, A. Hastings, and J. Largier (2003), Wind strength and biological productivity in upwelling systems: An idealized study, *Fish. Oceanogr.*, 12(4-5), 245–259.
- Chhak, K., and E. Di Lorenzo (2007), Decadal variations in the California Current upwelling cells, *Geophys. Res. Lett.*, 34, L14604, doi:10.1029/2007GL030203.
- Collins, M., *et al.* (2010), The impact of global warming on the tropical Pacific Ocean and El Niño, *Nat. Geosci.*, 3(6), 391–397.
- Cury, P., and C. Roy (1989), Optimal environmental window and pelagic fish recruitment success in upwelling areas, *Can. J. Fish. Aquat. Sci.*, 46(4), 670–680.
- Deser, C., A. Phillips, V. Bourdette, and H. Teng (2012), Uncertainty in climate change projections: The role of internal variability, *Clim. Dyn.*, 38(3-4), 527–546.
- Deser, C., A. S. Phillips, M. A. Alexander, and B. V. Smoliak (2014), Projecting North American climate over the next 50 years: Uncertainty due to internal variability*, *J. Clim.*, 27(6), 2271–2296.
- Di Lorenzo, E., A. J. Miller, N. Schneider, and J. C. McWilliams (2005), The warming of the California current system: Dynamics and ecosystem implications, *J. Phys. Oceanogr.*, 35(3), 336–362.
- Dorman, C. E., and C. D. Winant (1995), Buoy observations of the atmosphere along the West Coast of the United States, 1981-1990, *J. Geophys. Res.*, 100(C8), 16,029–16,044.

- Engida, Z., A. Monahan, D. Ianon, and R. E. Thomson (2016), Remote forcing of subsurface currents and temperatures near the Northern limit of the California Current System, *J. Geophys. Res. Oceans*, *121*, 7244–7262, doi:10.1002/2016JC011880.
- García-Reyes, M., and J. Largier (2010), Observations of increased wind-driven coastal upwelling off Central California, *J. Geophys. Res.*, *115*, C04011, doi:10.1029/2009JC005576.
- García-Reyes, M., W. J. Sydeman, S. A. Thompson, B. A. Black, R. R. Rykaczewski, J. A. Thayer, and S. J. Bograd (2013), Integrated assessment of wind effects on Central California's pelagic ecosystem, *Ecosystems*, *16*(5), 722–735.
- García-Reyes, M., J. L. Largier, and W. J. Sydeman (2014), Synoptic-scale upwelling indices and predictions of phyto- and zooplankton populations, *Prog. Oceanogr.*, *120*, 177–188.
- García-Reyes, M., W. J. Sydeman, D. S. Schoeman, R. R. Rykaczewski, B. A. Black, A. J. Smit, and S. J. Bograd (2015), Under pressure: Climate change, upwelling, and eastern boundary upwelling ecosystems, *Front. Mar. Sci.*, *2*, 109.
- Gruber, N. (2011), Warming up, turning sour, losing breath: Ocean biogeochemistry under global change, *Philos. Trans. R. Soc. A*, *369*(1943), 1980–1996.
- Hawkins, E., and R. Sutton (2009), The potential to narrow uncertainty in regional climate predictions, *Bull. Am. Meteorol. Soc.*, *90*(8), 1095–1107.
- Huyer, A. (1983), Coastal upwelling in the California current system, *Prog. Oceanogr.*, *12*(3), 259–284.
- Jacox, M., A. Moore, C. Edwards, and J. Fiechter (2014), Spatially resolved upwelling in the California Current System and its connections to climate variability, *Geophys. Res. Lett.*, *41*, 3189–3196, doi:10.1002/2014GL059589.
- Jacox, M. G., E. L. Hazen, and S. J. Bograd (2016), Optimal environmental conditions and anomalous ecosystem responses: Constraining bottom-up controls of phytoplankton biomass in the California current system, *Sci. Rep.*, *6*, 27612, doi:10.1038/srep27612.
- Kay, J., et al. (2015), The community earth system model (CESM) large ensemble project: A community resource for studying climate change in the presence of internal climate variability, *Bull. Am. Meteorol. Soc.*, *96*(8), 1333–1349.
- Lovenduski, N. S., G. A. McKinley, A. R. Fay, K. Lindsay, and M. C. Long (2016), Partitioning uncertainty in ocean carbon uptake projections: Internal variability, emission scenario, and model structure, *Global Biogeochem. Cycles*, *30*(9), 1276–1287.
- Lu, J., G. A. Vecchi, and T. Reichler (2007), Expansion of the Hadley cell under global warming, *Geophys. Res. Lett.*, *34*, L06805, doi:10.1029/2006GL028443.
- Lynn, R. J., S. J. Bograd, T. K. Chereskin, and A. Huyer (2003), Seasonal renewal of the California Current: The spring transition off California, *J. Geophys. Res.*, *108*(C8), 3279, doi:10.1029/2003JC001787.
- Marchesiello, P., and P. Estrade (2010), Upwelling limitation by onshore geostrophic flow, *J. Mar. Res.*, *68*(1), 37–62.
- McKinley, G. A., D. J. Pilcher, A. R. Fay, K. Lindsay, M. C. Long, and N. S. Lovenduski (2016), Timescales for detection of trends in the ocean carbon sink, *Nature*, *530*(7591), 469–472.
- Narayan, N., A. Paul, S. Mulitza, and M. Schulz (2010), Trends in coastal upwelling intensity during the late 20th century, *Ocean Sci.*, *6*(3), 815–823.
- Nelson, C. S. (1977), Wind stress and wind stress curl over the California current, *Tech. Rep.*, Naval Postgraduate School, Monterey, Calif.
- Riahi, K., S. Rao, V. Krey, C. Cho, V. Chirkov, G. Fischer, G. Kindermann, N. Nakicenovic, and P. Rafaj (2011), RCP 8.5—A scenario of comparatively high greenhouse gas emissions, *Clim. Change*, *109*(1–2), 33–57.
- Rykaczewski, R. R., and D. M. Checkley (2008), Influence of ocean winds on the pelagic ecosystem in upwelling regions, *Proc. Natl. Acad. Sci. U.S.A.*, *105*(6), 1965–1970.
- Rykaczewski, R. R., and J. P. Dunne (2010), Enhanced nutrient supply to the California Current Ecosystem with global warming and increased stratification in an earth system model, *Geophys. Res. Lett.*, *37*, L21606, doi:10.1029/2010GL045019.
- Rykaczewski, R. R., J. P. Dunne, W. J. Sydeman, M. García-Reyes, B. A. Black, and S. J. Bograd (2015), Poleward displacement of coastal upwelling-favorable winds in the ocean's eastern boundary currents through the 21st century, *Geophys. Res. Lett.*, *42*, 6424–6431, doi:10.1002/2015GL064694.
- Ryther, J. H., et al. (1969), Photosynthesis and fish production in the sea. The production of organic matter and its conversion to higher forms of life vary throughout the world ocean, *Science*, *166*, 72–76.
- Small, R. J., E. Curchitser, K. Hedstrom, B. Kauffman, and W. G. Large (2015), The Benguela upwelling system: Quantifying the sensitivity to resolution and coastal wind representation in a global climate model*, *J. Clim.*, *28*(23), 9409–9432.
- Smith, R., et al. (2010), The Parallel Ocean Program (POP) reference manual: Ocean component of the Community Climate System Model (CCSM) and Community Earth System Model (CESM), Los Alamos National Laboratory Tech. Rep. LAUR-10-01853, 141 pp. [Available at www.cesm.ucar.edu/models/cesm1.0/pop2/doc/sci/POPRefManual.pdf.]
- Solomon, A., et al. (2011), Distinguishing the roles of natural and anthropogenically forced decadal climate variability: Implications for prediction, *Bull. Am. Meteorol. Soc.*, *92*(2), 141.
- Sydeman, W., M. García-Reyes, D. Schoeman, R. Rykaczewski, S. Thompson, B. Black, and S. Bograd (2014), Climate change and wind intensification in coastal upwelling ecosystems, *Science*, *345*(6192), 77–80.
- Thompson, D. W., E. A. Barnes, C. Deser, W. E. Foust, and A. S. Phillips (2015), Quantifying the role of internal climate variability in future climate trends, *J. Clim.*, *28*(16), 6443–6456.
- Thompson, S. A., W. J. Sydeman, J. A. Santora, B. A. Black, R. M. Suryan, J. Calambokidis, W. T. Peterson, and S. J. Bograd (2012), Linking predators to seasonality of upwelling: Using food web indicators and path analysis to infer trophic connections, *Prog. Oceanogr.*, *101*(1), 106–120.
- Timmermann, A., J. Oberhuber, A. Bacher, M. Esch, M. Latif, and E. Roeckner (1999), Increased El Niño frequency in a climate model forced by future greenhouse warming, *Nature*, *398*(6729), 694–697.
- Wang, D., T. C. Gouhier, B. A. Menge, and A. R. Ganguly (2015), Intensification and spatial homogenization of coastal upwelling under climate change, *Nature*, *518*(7539), 390–394.
- Yin, J. H. (2005), A consistent poleward shift of the storm tracks in simulations of 21st century climate, *Geophys. Res. Lett.*, *32*, L18701, doi:10.1029/2005GL023684.